Processing and Application of Ceramics 12 [3] (2018) 230–239
https://doi.org/10.2298/PAC1803230K

Co-extrusion of zirconia core-shell rods with controlled porosity in the core

Jaroslav Kastyl*, Vaclav Pouchly, Martin Trunec

CEITEC BUT, Central European Institute of Technology, Brno University of Technology, Purkynova 123, 612 00 Brno, Czech Republic

Received 26 April 2018; Received in revised form 20 July 2018; Accepted 10 August 2018

Abstract

A method for manufacturing bi-layered zirconia rods of core-shell geometry with a porous core and a dense shell has been developed. Core-shell rods were successfully prepared by thermoplastic co-extrusion of assembled feed rods composed of core and shell zirconia feedstocks. Rheological analysis and adjustment of the feedstock viscosities enabled co-extrusion of regular core-shell rods of uniform shell thickness. Tapioca starch was used as a pore-forming agent in the core feedstock. Binder removal and high temperature treatment had to be modified in order to safely remove the starch particles. Sintering analysis revealed constrained sintering of porous cores in the core-shell rods due to the rigid dense shell, which resulted in an increased porosity in the core. Defect-free core-shell rods with a core porosity of up to 40% and different thicknesses of the dense shell were prepared.

Keywords: *core-shell, zirconia, composites, extrusion, porosity*

I. Introduction

The progress in the ceramic area of materials science is intensified by the development of new composite structures that can improve the current materials properties and in some cases even provide new properties. The layered arrangement is a common structure in ceramic composites and bodies with such an arrangement can exhibit either regular or functionally-graded macrostructures [1]. A specific variant of layered composites is the bi-layer material structure with core-shell geometry. The structure with core-shell geometry has one material (core), often in the form of a sphere or rod, surrounded by a layer of the other material (shell). The ceramics of the core and the shell can differ in composition [2–4] or they can be of the same ceramic material but different porosity [5–8]. The core-shell structures can offer mechanical or functional properties that cannot be obtained with individual homogeneous ceramic materials, i.e. the core-shell structures can modify the properties of these homogeneous ceramics. The applications of ceramic core-shell parts are diverse and the particular composition and structure of the core-shell body depends on specific requirements of the intended application. For example, ceramic core-shell rods based on zirconia and/or other ceramic materials have been applied as PZT actuators [3], bioceramic implants with a bone structure [7–9], solid oxide fuel cells [10,11] or as oxygen separation membranes [12,13]. Such structures can be fabricated by many methods such as freeze casting [5,7,14,15], slip casting or extrusion followed by a coating process [6,16,17], electrophoretic deposition [18], and co-extrusion [3,4,19,20]. The last mentioned method, co-extrusion, exhibits many processing advantages such as simple production with excellent interface between the core and shell materials, low-cost production and better mechanical properties of co-extruded bodies compared with other shaping methods [16,21,22]. During ceramic extrusion, a ceramic paste, often referred to as feedstock, is pushed through a shaping nozzle. In the co-extrusion process, two or more feedstocks are extruded simultaneously. There are two basic possibilities of feedstock arrangement for ceramic co-extrusion: i) the multi-channel or multi-billet extrusion [16,23–25], and ii) co-extrusion of a preform, which is often referred to as feed rod, with serial [20,26–28] or parallel [3,4,19,29,30] ordering of feedstocks in the feed rod.

* Corresponding authors: tel: +420 541149710,
e-mail: *jaroslav.kastyl@ceitec.vutbr.cz*

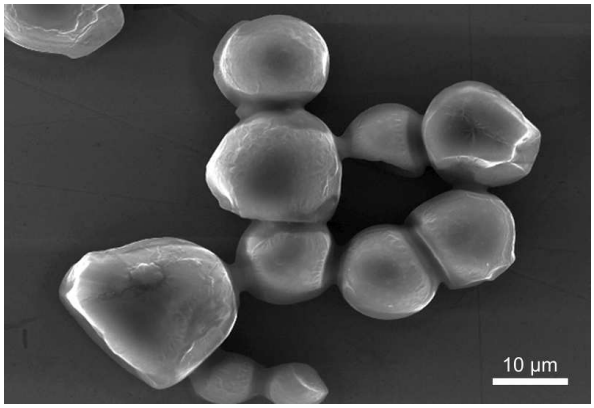

Figure 1. SEM micrograph of tapioca starch particles

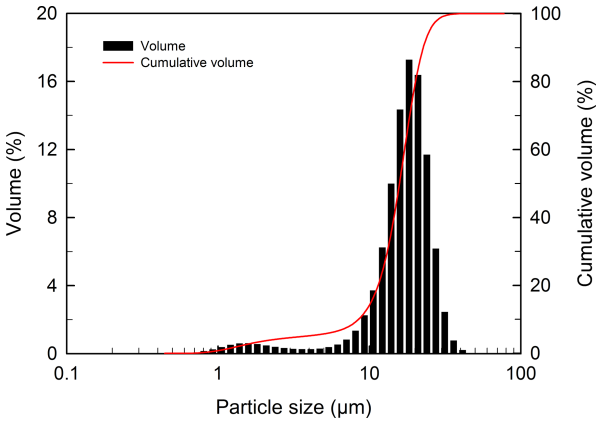

Figure 2. Particle size distribution of tapioca starch

Recently, Kastyl *et al.* [4] have reported on bi-material core-shell rods composed of dense zirconia toughened alumina (ZTA) core and dense alumina shell that exhibited a combination of high surface hardness of alumina with high fracture force in bending that even exceeded the value of monolithic ZTA. The reported bi-layer rods of core-shell geometry were successfully prepared by thermoplastic co-extrusion of assembled feed rods. A rheological description of the co-extrusion process and the demands on the feedstocks for a successful thermoplastic co-extrusion of ZTA/alumina core-shell rods have also been presented [4]. The core-shell rods with controlled porosity in the core represent another promising material structure that can benefit not only from the modified mechanical behaviour [5,7,8,14] but, in some cases, even from their interesting functional properties and behaviour [11,17,24]. Recently, Choi *et al.* [20] have reported on co-extrusion of core-shell rods with porous cores of variable size. Powell and Blackburn [24,25] have presented a detailed report on co-extrusion of multi-layered dense/porous ceramic microtubes. However, to the best of our knowledge, only very few studies concerning thermal co-extrusion of core-shell rods with porous cores have been reported. Therefore, the aim of this work is to investigate the key steps in the processing of ceramic core-shell rods with porous cores by the thermoplastic co-extrusion method. For this purpose, we prepared bi-layer zirconia core-shell rods with different volumes of porosity in the cores and with three various thicknesses of the dense shells.

II. Experimental

2.1. Materials and sample preparation

Zirconia powder stabilized with 3 mol% of Y_2O_3 (TZ-3YS-E, Tosoh, Japan) with a specific surface area of 6.8 m^2/g was used for the preparation of both the dense shells and the porous cores of the core-shell rods. Tapioca starch (Farmer Brand, Thailand) with narrow particle size distribution, median particle size (d_{50}) of 15.5 µm and near spherical particle morphology was used as a pore-forming agent. The SEM image and size distribution of starch particles are shown in Figs. 1 and 2, respectively. A thermoplastic binder system based on our previous experience [4,31,32] was composed of ethylene-vinyl acetate (EVA) copolymer (Elvax 250, Du Pont de Nemours, USA) and paraffin wax (R-54/56, Slovnaft, Slovakia). Stearic acid (1.0067, Merck, Germany) was used as a surfactant. The thermoplastic feedstocks were prepared by mixing ceramic powder with organic components in a two-blade high-shear kneader (HKD 0.6T, IKA-Werke, Germany) at a temperature of 120 °C for 2 h. The feedstocks were prepared as starch-free (referred to as Z) or filled with starch (referred to as ZST). The feedstock composition overview and feedstock abbreviations are summarized in Table 1. The volume ratio of zirconia to binder (EVA, paraffin, and stearic acid) in Z50 and ZST feedstocks was the same. The core-shell rods were co-extruded by piston extrusion of thermoplastic feed rods (preforms assembled from the core and shell feedstocks). In feed rods, the shell was applied manually on an extruded core as a plastic formable feedstock (not sprayed or dip-coated) and machined using a milling machine to obtain a regular shape of the preform (see the processing diagram in Fig. 3). Thus, we obtained a core-shell feed rod that could be inserted in the barrel of the extruder and co-extruded through the shaping nozzle. The core-shell rods were co-extruded with zirconia starch-filled feedstocks (ZST) in the core and surrounded by the shell of the zirconia starch-free Z50 feedstock. The selection of the Z50 feedstock for the shell is justified below in the Results and discussion section. Co-extrusion was carried out using a capillary rheometer (Galaxy V, Kayeness, USA) equipped with a conical nozzle with an inlet diameter of 9.55 mm and an outlet diameter of 3 mm that ended in a 12.5 mm long cylindrical part. The extrusion rate was 716 mm^3/min. The extrusion temperature was 120 °C and the rod was extruded into distilled water with the water level 3 mm below the nozzle outlet. The temperature of the water was 23 °C in order to solidify the plastic material as quickly as possible and prevent any shape deformation of the extruded rods. For comparison, non-layered dense and porous rods were also prepared, using the same extrusion parameters as used for the core-shell rods. All extruded

Table 1. Composition of ceramic feedstocks

Feedstock	ZrO_2		Tapioca starch		EVA		Paraffin wax		Stearic acid	
	[vol.%]	[wt.%]	[vol.%]	[wt.%]	[vol.%]	[wt.%]	[vol.%]	[wt.%]	[vol.%]	[wt.%]
Z48	48.0	85.71	-	-	25.4	7.09	17.7	4.73	8.9	2.47
Z50	50.4	86.86	-	-	23.7	6.38	16.5	4.25	9.4	2.51
Z52	52.0	87.55	-	-	22.6	5.95	15.7	3.97	9.7	2.53
Z55	55.0	88.81	-	-	20.5	5.18	14.3	3.45	10.2	2.56
ZST5	47.9	84.95	5.0	2.20	22.5	6.24	15.7	4.16	8.9	2.45
ZST10	45.4	82.92	10.0	4.54	21.3	6.09	14.8	4.06	8.5	2.39
ZST20	39.7	77.83	21.4	10.40	18.6	5.71	13.0	3.81	7.3	2.25
ZST30	35.3	73.41	30.0	15.49	16.6	5.39	11.6	3.59	6.5	2.12
ZST40	30.3	67.59	40.0	22.19	14.2	4.96	9.9	3.31	5.6	1.95
ZST50	25.2	60.85	50.0	29.95	11.8	4.47	8.3	2.98	4.7	1.75

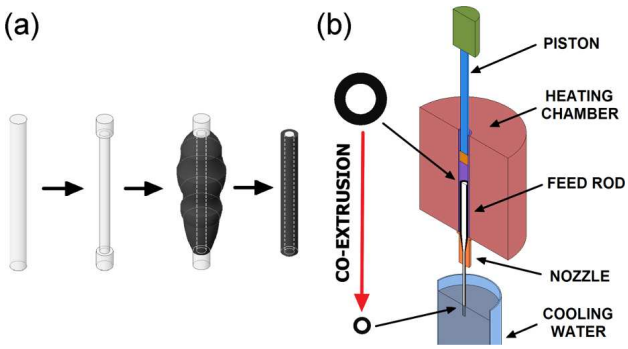

Figure 3. Diagram of (a) the feed rod preparation and (b) co-extrusion process

and co-extruded rods were cut into 50 mm long test pieces.

The thermoplastic binder was removed from the extruded rods in a nitrogen atmosphere at a heating rate of 10 °C/h, up to a temperature of 500 °C. Moreover, the heating rate was slowed down to 1 °C/h in the interval from 100 to 130 °C and a dwell time of 50 h at 130 °C was included. In order to obtain bodies with a sufficient handling strength, the debinding step was finished by heating up to 800 °C at a heating rate of 120 °C/h. During debinding, all the bodies were embedded in a granular activated carbon (AY-5 12×30, Carbon Link, Wigan, U.K.) to obtain more uniform binder removal [33–35]. Samples containing starch (porous non-layered rods and core-shell rods) were additionally heat-treated after the debinding step at a rate of 50 °C/h up to a temperature of 900 °C in an air atmosphere in order to completely remove all organic residues after the debinding process. Sintering took place in an air atmosphere at a temperature of 1500 °C for 2 h. The heating to the sintering temperature was at a rate of 300 °C/h up to a temperature of 1200 °C and then at a rate of 100 °C/h up to 1500 °C.

2.2. Characterization and evaluation methods

A capillary rheometer (Galaxy V, Kayeness, USA) with a capillary diameter of 1 mm and a length of 30 mm was used to examine the apparent viscosity of thermoplastic feedstocks. The rheological measurements were performed at shear rates from 1 to 500 1/s at a temperature ranging from 100 to 140 °C. The shear rate values were corrected to the non-Newtonian behaviour of the feedstocks according to the Weissenberg-Rabinowitsch method, using the KARS rheometer software.

The shell thickness and its geometric regularity in the feed rods, co-extrudates, and sintered core-shell samples were examined using a digital optical microscope (Dino-Lite Edge AM4115ZTL, AnMo, Taiwan). Thermogravimetric analyses (TGA) were performed using a TG analyser (96 Line TGA – DTA / DSC, Setaram, France) up to a temperature of 800 °C, using two heating rates and different atmospheres, always with a gas flow of 50 ml/min. The analysis at a heating rate of 10 °C/min in argon was used for green (extruded) samples to determine the decomposition progress. A low heating rate of 0.5 °C/min in argon was used for the starch analyses to determine the exact decomposition temperatures of starch. Moreover, a low heating rate of 0.5 °C/min in air was used for debound samples to determine the burn-out of organic residues after binder removal.

The bulk densities of sintered bodies were determined in accordance with the EN 623-2 standard, using the Archimedes method [36] in distilled water, always for at least three samples. The relative sample density was calculated using a theoretical density (TD) of 6.08 g/cm^3 for t-ZrO_2.

The presence of surface defects (pores, cracks, or delamination) in the core-shell bodies was determined using the penetration test with a penetration liquid (Indikal I, Druchema, the Czech Republic). The microstructures were investigated via scanning electron microscopy (SEM), using an XL30 microscope (Philips, the Netherlands).

III. Results and discussion

3.1. Rheological properties and co-extrusion process

The rheological behaviour of all investigated thermoplastic feedstocks at the extrusion temperature of 120 °C is compared in Fig. 4. With a starch addition to the basic 50 vol.% zirconia feedstock (Z50) the viscosity increased only slightly. It was found that even a starch addition of 40 vol.% provided a feedstock (ZST40) of reasonable viscosity that was lower than the viscosity of pure zirconia feedstock with 52 vol.% powder load-

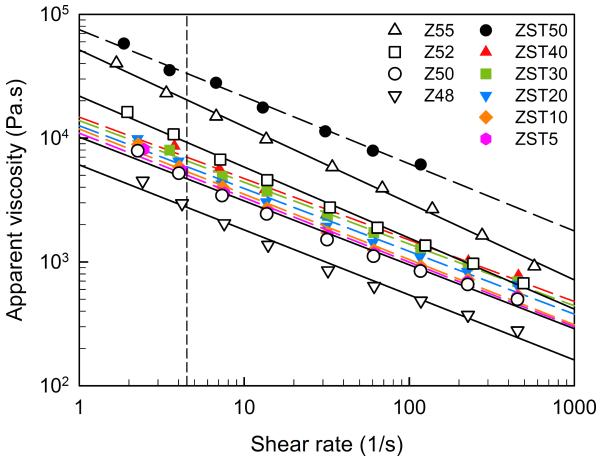

Figure 4. Apparent viscosity of feedstocks as a function of the shear rate at a temperature of 120 °C (full lines and long dashed lines represent the power law model for starch-free feedstocks (empty symbols) and starch-filled feedstocks (filled symbols), respectively, whereas the short dashed line indicates the maximum shear rate developed in the extrusion process)

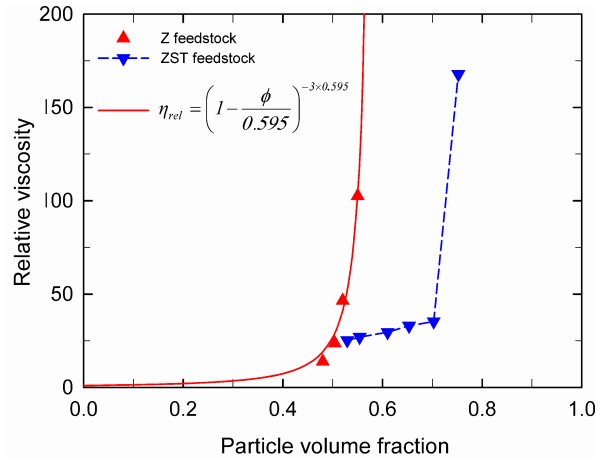

Figure 5. Relative viscosity of feedstocks as a function of particle volume fraction at 120 °C and a shear rate of 4.5 1/s (the full line represents the model according to Eq. 1 and the dashed line serves as a guide for eyes)

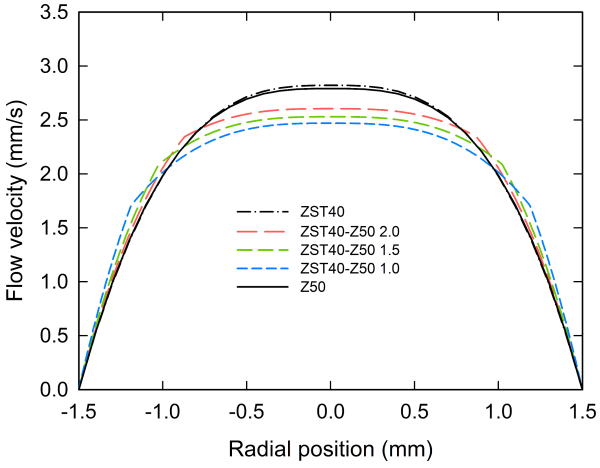

Figure 6. Flow velocity profiles in the nozzle during co-extrusion

ing (Z52). Although starch particles can be regarded as solids (there is no deformation of starch particles during mixing and extrusion), the multimodal nature of zirconia and starch particles enabled such a high loading with a still reasonable viscosity (Fig. 5). Only with the addition of 50 vol.% starch (ZST50) did the viscosity increase dramatically and the feedstock approached the critical point of loading. This feedstock could not be measured below 120 °C because it was losing its plastic behaviour. The pure zirconia feedstocks conformed to the Krieger-Dougherty relation for the dependence of relative viscosity, η_{rel}, on the powder loading, ϕ [37]:

$$\eta_{rel} = \frac{\eta}{\eta_0} = \left(1 - \frac{\phi}{\phi_{max}}\right)^{-[\eta]\phi_{max}} \quad (1)$$

where η is the apparent viscosity of the feedstock, η_0 is the viscosity of the binder, ϕ_{max} is the critical volume fraction, and $[\eta]$ is the intrinsic viscosity. On the contrary, the viscosity dependence of starch-filled feedstocks on solid loading could not be described with any reasonable model (Fig. 5).

All feedstocks behaved pseudoplastically, i.e. the viscosity decreased with increasing shear rate. In the range of investigated shear rates, the rheological behaviour of all feedstocks could be satisfactorily described ($R^2 > 0.96$) using the power law model [38]:

$$\eta = K \cdot \dot{\gamma}^{n-1} \quad (2)$$

where K is the consistency index, $\dot{\gamma}$ is the shear rate, and n is the power-law index giving the measure of pseudoplasticity (for $n < 1$ showing a more pronounced shear-thinning behaviour). The power law indexes, n, were almost similar for all feedstocks, close to the value of 0.5 and they are listed in Table 2. The dependence of feedstock viscosity on temperature was evaluated using the activation energy of viscous flow, E_a. The calculation was carried out using the Arrhenius-Andrade equation [38]:

$$\eta = A_0 \exp\left(\frac{E_a}{R \cdot T}\right) \quad (3)$$

Table 2. Rheological properties of ceramic feedstocks

Feedstock	η^* [kPa·s]	n	E_a [kJ/mol]
Z48	2.76	0.48	21.5
Z50	4.69	0.48	25.3
Z52	9.22	0.43	33.8
Z55	20.3	0.38	31.3
ZST5	5.00	0.48	24.0
ZST10	5.34	0.48	22.7
ZST20	5.86	0.49	21.2
ZST30	6.54	0.50	22.1
ZST40	7.00	0.50	23.2
ZST50	33.3	0.46	N/A

*Viscosity, η is presented at a shear rate of 4.5 1/s and 120 °C

where A_0 is the frequency term, R is the universal gas constant, and T is the absolute temperature. The calculation was performed for a shear rate of 4.5 1/s, which is the estimated wall shear rate in the extrusion nozzle. The values of E_a ranged between 21 and 25 kJ/mol, and there was only a small decrease in activation energies with the addition of starch (i.e. the viscosities of starch-filled feedstocks are slightly less sensitive to the temperature changes than the viscosities of pure zirconia feedstocks).

In our previous work on co-extrusion [4], we have shown and explained the benefits of using the shell feedstock with a lower viscosity than that of the core feedstock. This was taken into consideration in all experiments reported here, where the viscosity of the shell feedstock (Z50) was always lower than that of the core feedstocks (ZST20, ZST30, and ZST40). Such a feedstock arrangement provided uniform and more plug-like velocity profiles in the extrusion nozzle. The velocity profile of flow in a nozzle, $v(r)$, can be expressed as [39]:

$$v(r) = \left(\frac{\tau}{K \cdot R}\right)^{\frac{1}{n}} \frac{n}{n+1}\left[R^{\frac{n+1}{n}} - r^{\frac{n+1}{n}}\right] \tag{4}$$

where τ is the shear stress, R is the nozzle radius, and r is the radial position. In the case of co-extrusion, the velocity profiles in the shell and in the core have to be calculated separately for each component as [39]:

$$v_c(r) = \left(\frac{\tau}{K_c \cdot R}\right)^{\frac{1}{n_c}} \frac{n_c}{n_c+1}\left[R_i^{\frac{n_c+1}{n_c}} - r^{\frac{n_c+1}{n_c}}\right] + \\ + \left(\frac{\tau}{K_s \cdot R}\right)^{\frac{1}{n_s}} \frac{n_s}{n_s+1}\left[R^{\frac{n_s+1}{n_s}} - R_i^{\frac{n_s+1}{n_s}}\right] \tag{5}$$

and

$$v_s(r) = \left(\frac{\tau}{K_s \cdot R}\right)^{\frac{1}{n_s}} \frac{n_s}{n_s+1}\left[R^{\frac{n_s+1}{n_s}} - r^{\frac{n_s+1}{n_s}}\right] \tag{6}$$

where the subscripts c and s stand for the core and the shell, respectively, and R_i refers to the radial position of the interface between the core and the shell feedstock. These equations can be solved using the approach derived in [4]. Figure 6 shows the calculated velocity profiles in the extrusion nozzle during co-extrusion experiments. The co-extrusion flow with the purposely modified velocity profiles enabled co-extrusion of regular core-shell rods of constant shell thicknesses. Figure 7 shows the shell thickness of the co-extruded rods (ZST40-Z50) prepared from three feed rods of different shell thicknesses, namely 1 mm (ZST40-Z50 1.0), 1.5 mm (ZST40-Z50 1.5), and 2 mm (ZST40-Z50 2.0). After the flow stabilization (first 50 mm of the co-extruded rod), the shell thickness of the core-shell rods was almost constant, with average thicknesses of 312, 477 and 630 µm for feed rods with shell thicknesses of 1, 1.5 and 2 mm, respectively. The measured shell thicknesses corresponded well with the theoretical thicknesses (calculated from the feed rod geometry and extrusion ratio) as shown in Fig. 7. Similar results were obtained also in the case of ZST20-Z50 and ZST30-Z50 core-shell rods.

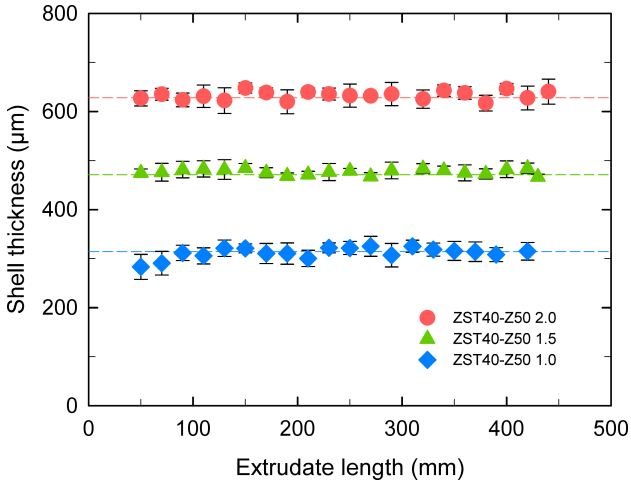

Figure 7. Shell thickness along the length of co-extruded core-shell rods (the dashed lines represent the theoretical shell thickness after feed rod co-extrusion, the error bars in the graph indicate the 99% confidence interval)

3.2. *Removal of the thermoplastic binder and pore-forming agent*

Removal of the feedstock binder had to be carried out in an inert nitrogen atmosphere in order to prevent any binder oxidation causing cracks and large pores in bodies during debinding [40]. To evaluate the decomposition processes, thermogravimetric analyses were performed. The thermogravimetric curves of starch, Z50 and ZST feedstocks in an inert atmosphere are shown in Fig. 8. The binder removal from the starch-free feedstock (Z50) took place in two main steps in temperature ranges of 240–350 °C and 420–480 °C. In the first step, paraffin, stearic acid and acetate side groups from the EVA copolymer were removed. In the second step,

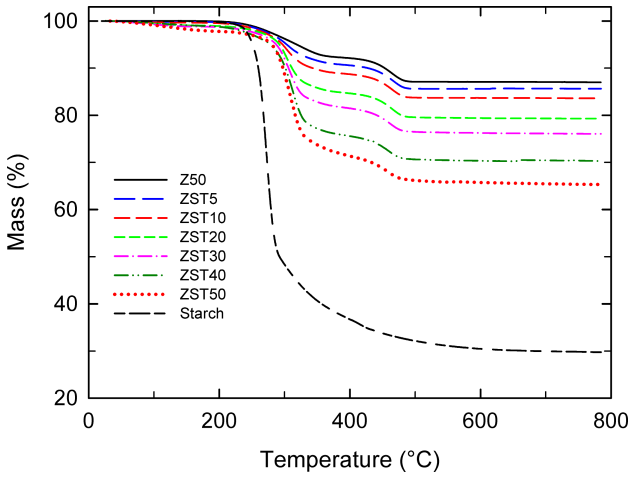

Figure 8. Mass loss of ceramic feedstocks and tapioca starch during heating in an inert atmosphere

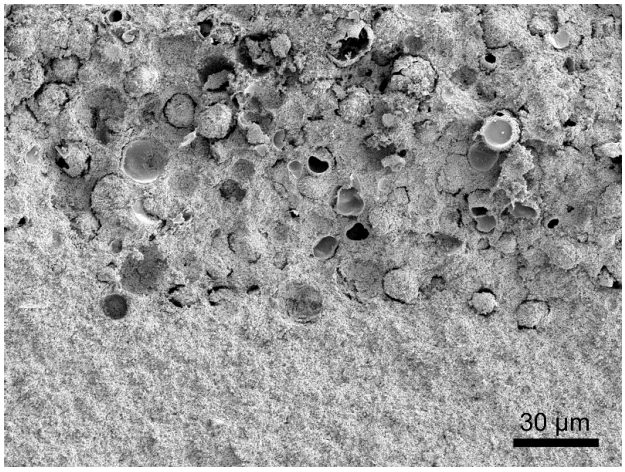

Figure 9. SEM image of the core-shell interface region on a fracture surface of ZST40-Z50 1.5 core-shell rod after debinding in an inert atmosphere

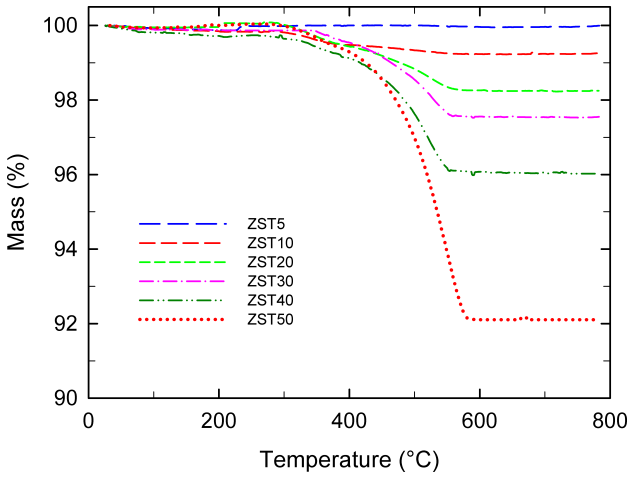

Figure 10. Mass loss of debound samples during heating in an oxidative atmosphere (air)

the rest of the EVA polymer was degraded and evaporated [35]. There were only negligible carbon residues remaining in the debound feedstock. In the feedstock filled with starch, the mass loss in the first debinding step increased because the starch degraded in a similar temperature range. Unfortunately, the thermal decomposition (pyrolysis) of starch into volatile components is not complete in an inert atmosphere and about 30 wt.% of the degraded starch residues remained after heating the pure starch in an inert atmosphere. Although the thermal degradation of starch particles in ceramic samples was more pronounced than the degradation of pure starch, degraded starch residues could be found in the debound bodies. The micrograph in Fig. 9 shows the fracture surface of a core-shell body after debinding in an inert atmosphere. The partially degraded starch particles are clearly visible. These residues could be entirely removed during heating in an air atmosphere in the temperature range from 280 to 560 °C as proved by the thermogravimetric analysis in air (see Fig. 10). We found 1.75, 2.46 and 3.98 wt.% of the degraded starch residues in the debound ZST20, ZST30, and ZST40 ceramic samples, respectively. Such an amount of organic residues can be usually harmlessly removed during a standard sintering schedule in an air atmosphere [41]. However, in our core-shell structures, the dense shell without any open macro pores prevented an easy transport of volatile products from the porous centre to the body surroundings. A rapid gas evolution from the starch residues at a standard sintering rate of 300 °C/h caused a gas overpressure inside the core-shell sample. This overpressure resulted in cracks in the dense shell layer (Fig. 11). These defects were not observed in non-layered porous bodies (filled with starch but without the dense shell layer). Thus an annealing step in an air atmosphere at a low heating rate of 50 °C/h up to 900 °C had to be added prior to the sintering regime in order to safely remove all the starch residues from core-shell rods and obtain defect-free rods.

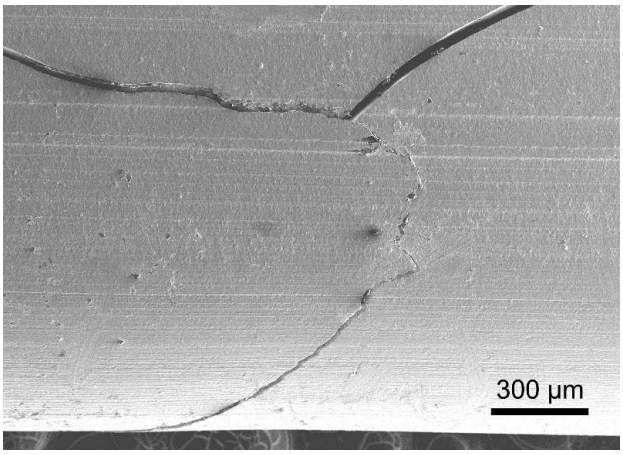

Figure 11. Cracks on the surface of the ZST40-Z50 1.5 rod sintered without the annealing step in an air prior to sintering

3.3. Sintering of core-shell rods and their structure

The cross-sections of sintered defect-free core-shell rods of different core porosities are shown in Fig. 12. High magnification images revealed clusters and peelings of sintered zirconia mass in the large pores of the core in the core-shell rods (Fig. 13). These clusters and peelings are ceramic particles that got stuck to the individual starch particles during feedstock processing or, more probably, during debinding, when the starch got melted. Ceramic particles formed a coating on the surface of the starch particle and peeled off from the ceramic mass during the degradation and removal of the starch particles. The first signs of peeling and separation can already be observed in a body after debinding in an inert atmosphere (Fig. 9). This phenomenon was also observed by other authors who used starch [42,43] or PMMA [44,45] particles as a pore-forming agent for the preparation of porous ceramics.

The dimensions and porosities of sintered non-layered dense and porous rods are given in Table 3. The dense rod (Z50) could be sintered to almost full density with only 0.7% of porosity. The porous non-

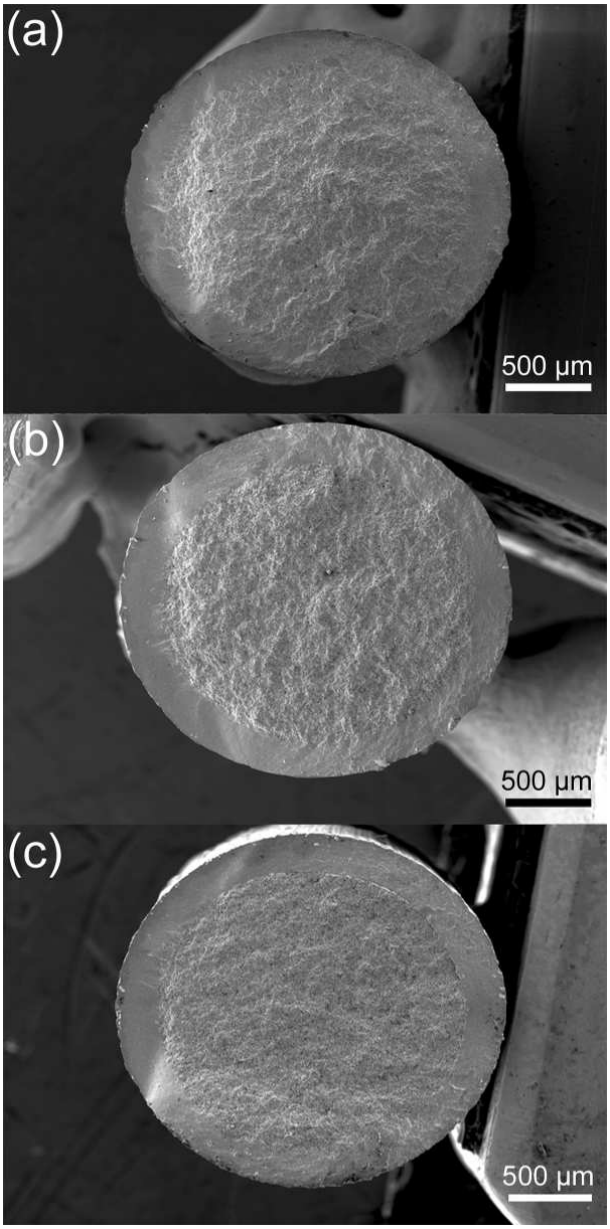

Figure 12. The cross sections (fracture surfaces) of: a) ZST20-Z50 1.0, b) ZST30-Z50 1.0 and c) ZST40-Z50 1.0 defect-free core-shell rods after sintering

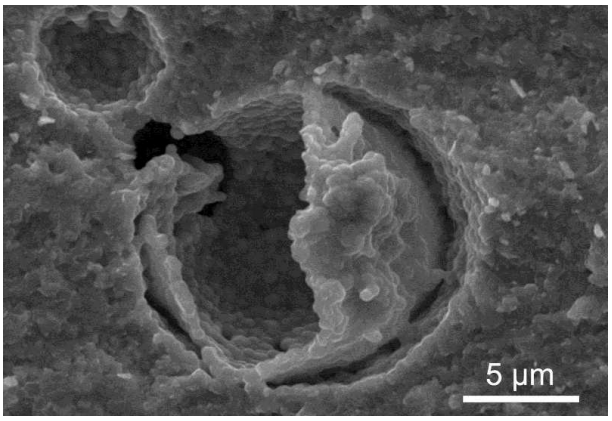

Figure 13. SEM micrograph of a sintered ceramic peeling in a pore formed by a starch particle

Table 3. Dimensions and densities of sintered non-layered rods

Sample	Diameter* [mm]	Bulk density* [g/cm^3]	Porosity [%]
Z50	2.38 ± 0.02	6.04 ± 0.02	0.7
ZST5	2.32 ± 0.01	5.77 ± 0.01	5.0
ZST10	2.32 ± 0.01	5.53 ± 0.01	9.0
ZST20	2.32 ± 0.01	4.92 ± 0.02	19.1
ZST30	2.31 ± 0.01	4.41 ± 0.03	27.5
ZST40	2.29 ± 0.01	3.89 ± 0.04	36.0
ZST50	2.29 ± 0.01	3.39 ± 0.01	44.2

*Average value is given with 99% confidence interval

layered rods (ZST) exhibited increasing porosity in dependence on the increasing starch content in the feedstock (Fig. 14). However, the final porosity in sintered rods was always lower than the porosity expected for the starch content in the feedstock and the difference increased with the starch loading. The diameter of sintered non-layered rods decreased from 2.38 mm for the dense rod (Z50) to 2.29 mm for the most porous rod (ZST50). These results suggest that the large pores (formed by the starch particles), which were two order of magnitude bigger than ceramic particles, could also be partially sintered and eliminated. This phenomenon was investigated by Slamovich and Lange [46], and thermodynamic and kinetic explanations were provided. Surprisingly, the diameters of sintered core-shell rods with porous cores (Table 4) were similar to the diameter of the non-layered dense rod. Figure 15 compares the sintering curves for non-layered and core-shell rods and shows that the shrinkage of core-shell rods was very close to the shrinkage of the non-layered dense rod, whereas the shrinkage of the non-layered porous rod was much bigger. From these results it follows that the shrinkage of the porous core in a core-shell rod was constrained during sintering, a phenomenon commonly observed in layered ceramic structures [47,48]. The core-shell rod with the most rigid shell (i.e. with the thickest

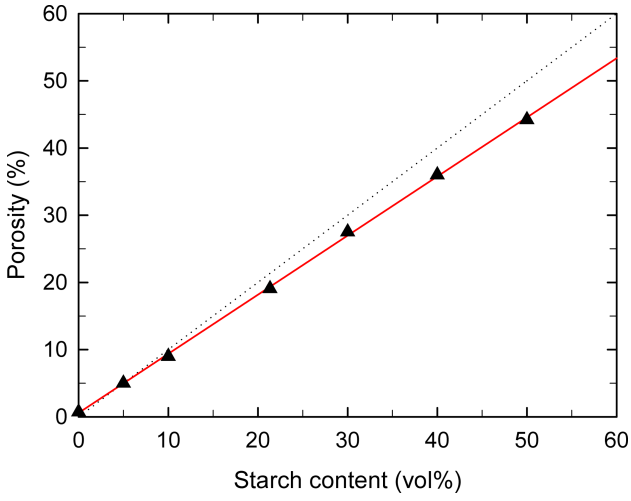

Figure 14. Dependence of porosity in sintered non-layered rods on starch loading in the feedstocks (the full line represents linear regression)

Table 4. Dimensions and densities of sintered core-shell rods

Sample	Diameter* [mm]	Shell thickness* [μm]	Bulk density* [g/cm^3]	Relative density [%TD]	Calculated core porosity [%]
ZST20-Z50 1.0	2.39 ± 0.01	256 ± 6	5.28 ± 0.03	86.9	20.6
ZST20-Z50 1.5	2.39 ± 0.01	365 ± 12	5.43 ± 0.07	89.3	21.2
ZST20-Z50 2.0	2.39 ± 0.01	517 ± 9	5.59 ± 0.03	92.0	23.0
ZST30-Z50 1.0	2.38 ± 0.01	270 ± 21	4.97 ± 0.04	81.7	30.0
ZST30-Z50 1.5	2.39 ± 0.01	392 ± 16	5.25 ± 0.03	86.4	29.0
ZST30-Z50 2.0	2.39 ± 0.01	509 ± 9	5.45 ± 0.03	89.6	29.8
ZST40-Z50 1.0	2.37 ± 0.01	259 ± 4	4.68 ± 0.04	76.9	37.2
ZST40-Z50 1.5	2.38 ± 0.01	376 ± 3	4.98 ± 0.03	81.8	37.8
ZST40-Z50 2.0	2.39 ± 0.01	520 ± 20	5.29 ± 0.03	87.0	39.0

*Average value is given with 99% confidence interval

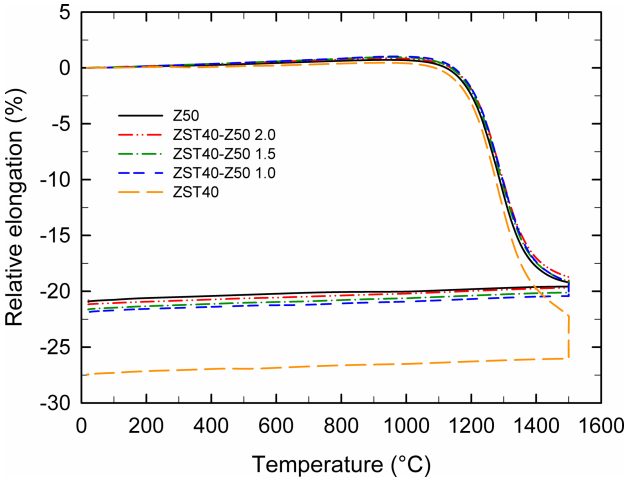

Figure 15. Shrinkage as a function of temperature for extruded non-layered (Z50 and ZST40) and co-extruded core-shell rods (ZST40-Z50) during sintering and subsequent cooling

shell) exhibited almost the same shrinkage as the fully dense rod. The core porosity, as calculated from the dimensions of the core-shell rods and shown in Table 4, confirmed the constrained sintering in porous cores of the core-shell rods. The calculated porosity in the core was close to the volume of starch in the feedstock, with the highest porosity which tends to be obtained in the core surrounded by the thickest shell. Despite the constrained sintering, no cracks were observed at the core-shell interface or in the core. Interesting mechanical behaviour of the zirconia co-extruded core-shell rods with porous core and dense shell, namely lowering of the Young's modulus without sacrificing the flexural strength of the rods, was investigated in our previous paper [49].

IV. Conclusions

The core-shell zirconia rods with porous cores and dense shells were successfully produced by piston co-extrusion of ceramic feed rods based on thermoplastic feedstocks. Tapioca starch was used as a pore-forming agent in the core feedstock. The shell feedstock was purposely prepared with a lower viscosity than the core feedstock. This arrangement enabled co-extrusion of regular core-shell rods of uniform shell thickness. The debinding process had to be modified to safely remove the residues after the starch degradation and removal in an inert atmosphere. The dense shell restricted the core shrinkage and caused a constrained sintering of the porous core, which resulted in higher porosity of the core. It was possible to prepare defect-free core-shell rods with a core porosity of up to 40% and a thickness of the dense shell ranging from 260 to 520 μm.

Acknowledgement: This research has been financially supported by the Ministry of Education, Youth and Sports of the Czech Republic under the project CEITEC 2020 (LQ1601).

References

1. T. Chartier, D. Merle, J.L. Besson, "Laminar ceramic composites", *J. Eur. Ceram. Soc.*, **15** [2] (1995) 101–107.
2. S. Bueno, B. Ferrari, C. Melandri, G. de Portu, C. Baudín, "Processing of alumina-coated tetragonal zirconia materials and their response to sliding wear", *Ceram. Int.*, **36** [5] (2010) 1545–1552.
3. C.-B. Yoon, S.-H. Jun, S.-M. Lee, H.-E. Kim, K.-W. Lee, "Piezoelectric fibers with uniform internal electrode by co-extrusion process", *J. Am. Ceram. Soc.*, **89** [4] (2006) 1333–1336.
4. J. Kastyl, Z. Chlup, F. Clemens, M. Trunec, "Ceramic core-shell composites with modified mechanical properties prepared by thermoplastic co-extrusion", *J. Eur. Ceram. Soc.*, **35** [10] (2015) 2873–2881.
5. C. Hong, J. Du, J. Liang, X. Zhang, J. Han, "Functionally graded porous ceramics with dense surface layer produced by freeze-casting", *Ceram. Int.*, **37** [8] (2011) 3717–3722.
6. Z. Chlup, D. Salamon, "Properties of porous multi-layered free-standing ceramic microchannels", *Scr. Mater.*, **63** [6] (2010) 597-600.
7. F. He, J. Ye, "Bi-layered calcium phosphate cement-based composite scaffold mimicking natural bone structure", *Sci. Technol. Adv. Mater.*, **14** [4] (2013) 045010.
8. F. Zhang, J. Chang, J. Lu, K. Lin, C. Ning, "Bioinspired structure of bioceramics for bone regeneration in load-bearing sites", *Acta Biomater.*, **3** [6] (2007) 896–904.
9. D.-W. Jang, T.-H. Nguyen, S.K. Sarkar, B.-T. Lee, "Microwave sintering and in vitro study of defect-free stable porous multilayered HAp-ZrO_2 artificial bone scaffold", *Sci. Technol. Adv. Mater.*, **13** [3] (2012) 035009.
10. T. Suzuki, Y. Funahashi, T. Yamaguchi, Y. Fujishiro, M.

Awano, "Development of fabrication/integration technology for micro tubular SOFCs", pp. 141–177 in: *Micro fuel cells*, Ed. T.S. Zhao, Academic Press, Boston, 2009.
11. T. Suzuki, Y. Funahashi, T. Yamaguchi, Y. Fujishiro, M. Awano, "Fabrication and characterization of micro tubular SOFCs for advanced ceramic reactors", *J. Alloy. Compd.*, **451** [1–2] (2008) 632–635.
12. H. Verweij, "Ceramic membranes: morphology and transport", *J. Mater. Sci.*, **38** [23] (2003) 4677–4695.
13. S.P.S. Badwal, F.T. Ciacchi, "Ceramic membrane technologies for oxygen separation", *Adv. Mater.*, **13** [12-13] (2001) 993–996.
14. Y.-M. Soon, K.-H. Shin, Y.-H. Koh, J.-H. Lee, W.-Y. Choi, H.-E. Kim, "Fabrication and compressive strength of porous hydroxyapatite scaffolds with a functionally graded core/shell structure", *J. Eur. Ceram. Soc.*, **31** [1-2] (2011) 13–18.
15. Y.F. Tang, K. Zhao, L. Hu, Z.X. Wu, "Two-step freeze casting fabrication of hydroxyapatite porous scaffolds with bionic bone graded structure", *Ceram. Int.*, **39** [8] (2013) 9703–9707.
16. B. Mani, M.H. Paydar, "Mechanical behaviour of multilayer half-cells of microtubular solid oxide fuel cells fabricated by the co-extrusion process", *Ceram. Int.*, **42** [3] (2016) 4194–4203.
17. W.-S. Hsieh, P. Lin, S.-F. Wang, "Fabrication of electrolyte supported micro-tubular SOFCs using extrusion and dip-coating", *Int. J. Hydrog. Energy*, **38** [6] (2013) 2859–2867.
18. C. Kaya, "Al_2O_3–Y-TZP/Al_2O_3 functionally graded composites of tubular shape from nano-sols using double-step electrophoretic deposition", *J. Eur. Ceram. Soc.*, **23** [10] (2003) 1655–1660.
19. D.-W. Jang, Y.-H. Kim, B.-T. Lee, "Microstructure control of TCP/TCP-(t-ZrO_2)/t-ZrO_2 composites for artificial cortical bone", *Mater. Sci. Eng. C-Mater. Biol. Appl.*, **31** [8] (2011) 1660–1666.
20. I.-J. Choi, Y.-W. Moon, Y.-H. Koh, H.-E. Kim, "Novel three-dimensional extrusion of multilayered ceramic/camphene mixture for gradient porous ceramics", *J. Am. Ceram. Soc.*, **99** [2] (2016) 395–398.
21. K. Kendall, "Progress in microtubular solid oxide fuel cells", *Int. J. Appl. Ceram. Technol.*, **7** [1] (2010) 1–9.
22. A. Peled, S.P. Shah, "Processing effects in cementitious composites: Extrusion and casting", *J. Mater. Civ. Eng.*, **15** [2] (2003) 192–199.
23. Z. Chen, K. Ikeda, T. Murakami, T. Takeda, J.-X. Xie, "Fabrication of composite pipes by multi-billet extrusion technique", *J. Mater. Process. Technol.*, **137** [1-3] (2003) 10–16.
24. J. Powell, S. Blackburn, "Co-extrusion of multilayered ceramic micro-tubes for use as solid oxide fuel cells", *J. Eur. Ceram. Soc.*, **30** [14] (2010) 2859–2870.
25. J. Powell, S. Blackburn, "The unification of paste rheologies for the co-extrusion of solid oxide fuel cells", *J. Eur. Ceram. Soc.*, **29** [5] (2009) 893–897.
26. K. Bhowmick, D. Furniss, H.P. Morvan, A.B. Seddon, T.M. Benson, "Predictive, miniature co-extrusion of multilayered glass fiber-optic preforms", *J. Am. Ceram. Soc.*, **99** [1] (2016) 106–114.
27. K. Bhowmick, H.P. Morvan, D. Furniss, A.B. Seddon, T.M. Benson, "Co-extrusion of multilayer glass fiber-optic preforms: Prediction of layer dimensions in the extrudate", *J. Am. Ceram. Soc.*, **96** [1] (2013) 118–124.
28. J. Dooley, *Viscoelastic Flow Effects in Multilayer Polymer Coextrusion*, PhD thesis, Technische Universiteit Eindhoven, Eindhoven, 2002.
29. Y.-H. Koh, H.-W. Kim, H.-E. Kim, J.W. Halloran, "Fabrication and compressive strength of macrochannelled tetragonal zirconia polycrystals with calcium phosphate coating layer", *J. Mater. Res.*, **18** [09] (2003) 2009–2012.
30. Y.-W. Moon, K.-H. Shin, Y.-H. Koh, S.-W. Yook, C.-M. Han, H.-E. Kim, "Novel ceramic/camphene-based co-extrusion for highly aligned porous alumina ceramic tubes", *J. Am. Ceram. Soc.*, **95** [6] (2012) 1803–1806.
31. M. Trunec, J. Cihlar, S. Diethelm, J. Van Herle, "Tubular $La_{0.7}Ca_{0.3}Fe_{0.85}Co_{0.15}O_{3-\delta}$ perovskite membranes, Part I: Preparation and properties", *J. Am. Ceram. Soc.*, **89** [3] (2006) 949–954.
32. K. Maca, M. Trunec, J. Cihlar, "Injection moulding and sintering of ceria ceramics", *Ceram. Int.*, **28** [3] (2002) 337–344.
33. M. Trunec, J. Cihlar, "Removal of thermoplastic binders from ceramic green bodies", *Ceramics-Silikáty*, **41** [2] (1997) 67–80.
34. M. Trunec, J. Cihlar, "Effect of activated carbon bed on binder removal from ceramic injection moldings", *J. Am. Ceram. Soc.*, **84** [3] (2001) 675–677.
35. M. Trunec, J. Cihlar, "Thermal removal of multicomponent binder from ceramic injection mouldings", *J. Eur. Ceram. Soc.*, **22** [13] (2002) 2231-2241.
36. ČSN EN 623-2:1993 "Advanced technical ceramics - monolithic ceramics - general and textural properties - part 2: determination of density and porosity". Czech version of the EN 623-2:1993. *Czech Standards Institute*.
37. I.M. Krieger, T.J. Dougherty, "A mechanism for non-Newtonian flow in suspensions of rigid spheres", *Trans. Soc. Rheo.*, **3** [1] (1959) 137-152.
38. A.V. Shenoy, *Rheology of filled polymer systems*, 1st edition. Kluwer Academic Publishers, Dordrecht, 1999.
39. C.D. Han, *Multiphase flow in polymer processing*, 1st edition. Academic Press, New York, 1981.
40. M. Trunec, J. Cihlář, "Thermal debinding of injection moulded ceramics", *J. Eur. Ceram. Soc.*, **17** [2-3] (1997) 203–209.
41. M.N. Rahaman, *Ceramic Processing and Sintering*, 2nd edition. Routledge, New York, 2003.
42. L.B. Garrido, M.P. Albano, K.P. Plucknett, L. Genova, "Effect of starch filler content and sintering temperature on the processing of porous 3Y-ZrO_2 ceramics", *J. Mater. Process. Technol.*, **209** [1] (2009) 590–598.
43. M.P. Albano, L.B. Garrido, K. Plucknett, L.A. Genova, "Processing of porous yttria-stabilized zirconia tapes: Influence of starch content and sintering temperature", *Ceram. Int.*, **35** [5] (2009) 1783–1791.
44. R. Liu, C.-a. Wang, "Effects of mono-dispersed PMMA micro-balls as pore-forming agent on the properties of porous YSZ ceramics", *J. Eur. Ceram. Soc.*, **33** [10] (2013) 1859–1865.
45. J. Zhou, C.-A. Wang, "Porous yttria-stabilized zirconia ceramics fabricated by nonaqueous-based gelcasting process with PMMA microsphere as pore-forming agent", *J. Am. Ceram. Soc.*, **96** [1] (2013) 266–271.
46. E.B. Slamovich, F.F. Lange, "Densification of large pores: II, Driving potentials and kinetics", *J. Am. Ceram. Soc.*, **76** [6] (1993) 1584–1590.
47. K. Maca, V. Pouchly, D. Drdlik, H. Hadraba, Z.

Chlup, "Dilatometric study of anisotropic sintering of alumina/zirconia laminates with controlled fracture behaviour", *J. Eur. Ceram. Soc.*, **37** [14] (2017) 4287–4295.
48. T.T. Molla, D.K. Ramachandran, D.W. Ni, V. Esposito, F. Teocoli, E. Olevsky, R. Bjørk, N. Pryds, A. Kaiser, H.L. Frandsen, "Modeling constrained sintering of bi-layered tubular structures", *J. Eur. Ceram. Soc.*, **35** [3] (2015) 941–950.
49. J. Kastyl, Z. Chlup, F. Clemens, M. Trunec, "Mechanical properties of zirconia core-shell rods with porous core and dense shell prepared by thermoplastic co-extrusion", *J. Eur. Ceram. Soc.*, **37** [6] (2017) 2439–2447.